Inorganic Chemistry

Article

pubs.acs.org/IC

Neutron Diffraction Study of the Li-Ion Battery Cathode $Li_2FeP_2O_7$

Prabeer Barpanda,*[,†,‡,⊥] Gwenaëlle Rousse,[§,⊥] Tian Ye,[†] Chris D. Ling,[∥] Zakiah Mohamed,[∥] Yannick Klein,[§] and Atsuo Yamada[†,‡]

[†]Department of Chemical System Engineering, The University of Tokyo, 7-3-1 Hongo, Bunkyo-ku, Tokyo 113-8656, Japan

[‡]Unit of Element Strategy Initiative for Catalysts & Batteries, ESICB, Kyoto University, Kyoto 615-8510, Japan

[§]Institut de Minéralogie et de Physique des Milieux Condensés (IMPMC), CNRS UMR 7590, Université Pierre et Marie Curie (UPMC), Case Courrier 115, 4 Place Jussieu, 75252 Paris Cedex 05, France

[∥]School of Chemistry, The University of Sydney, Sydney, NSW 2006, Australia

ABSTRACT: With a combination of magnetic susceptibility measurements and low-temperature neutron diffraction analyses, the magnetic structure of $Li_2FeP_2O_7$ cathode has been solved. This pyrophosphate $Li_2FeP_2O_7$ compound stabilizes into a monoclinic framework (space group $P2_1/c$), having a pseudolayered structure with the constituent Li/Fe sites distributed into MO_6 and MO_5 building units. The magnetic susceptibility follows a Curie–Weiss behavior above 50 K. $Li_2FeP_2O_7$ shows a long-range antiferromagnetic ordering at T_N = 9 K, as characterized by the appearance of distinct additional peaks in the neutron diffraction pattern below T_N. Its magnetic reflections can be indexed with a propagation vector **k** = (0,0,0). The magnetic moments inside the FeO_6–FeO_5 clusters are ferromagnetic, whereas these clusters are antiferromagnetic along the chains. The adjacent chains are in turn ferromagnetically arranged along the *a*-axis. The magnetic structure of $Li_2FeP_2O_7$ cathode material is described focusing on their localized spin–spin exchange. The magnetic structure and properties have been generalized for $Li_2FeP_2O_7$–$Li_2CoP_2O_7$ binary solid solutions.

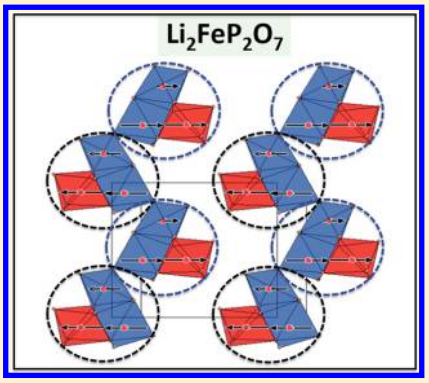

INTRODUCTION

Since Sony's commercialization of $LiCoO_2$/C rechargeable batteries (1991), Li-ion batteries have become the torch-bearer electrochemical energy storage devices widespread in the arena of portable electronics, (hybrid) electric vehicles, and remote grid storage.[1,2] The constant call for improved battery performance has propelled research efforts on optimizing existing cathodes (e.g., $LiCoO_2$, $LiMn_{3/2}Ni_{1/2}O_4$, $LiCo_{1/3}Mn_{1/3}Ni_{1/3}O_2$, $LiFePO_4$, etc.)[3−7] as well as unveiling newer cathode candidates.[8] The latter quest has unraveled many polyanionic cathodes like borates ($LiMBO_3$), silicates (Li_2MSiO_4), fluorophosphates ($LiMPO_4F$), and fluorosulphate ($LiMSO_4F$), etc.[9−13] Although some of these candidates have commercial potential, they are often limited by slow kinetics, cumbersome synthesis, ambient poisoning, and/or low redox voltage. From an application point-of-view, the PO_4-based systems have become the most suitable cathodes owing to their robust structure, ease of synthesis, economy, and robust thermal/chemical stability.

Moving over from $LiMPO_4$, the lithium metal pyrophosphates ($Li_{2-x}MP_2O_7$; M = 3d transition metals) with characteristic diphosphate (P_2O_7, i.e., PO_4–PO_4) units form a large family of cathodes with rich structural diversity and the widest range of redox potential (2.0–4.9 V).[14] The first pyrophosphate cathode ($LiFeP_2O_7$)[15] introduced by Goodenough (1997) was followed by numerous reports on $Li_{2-x}MP_2O_7$ (x = 0–1) pyrophosphate cathodes.[14] While most of them suffer from low voltage, Nishimura et al. reported $Li_2FeP_2O_7$ as a competent cathode showing highest redox potential (c.a. 3.5 V) among all Fe-containing PO_4-based systems. It comes with convenient synthesis, robust two-dimensional Li-diffusion pathways,[16,17] and a reversible capacity exceeding 100 mAh/g without the need of any cathode optimization.[18−21]

$Li_2FeP_2O_7$ has rekindled wide research into pyrophosphate cathodes leading to discovery of novel Li-based (e.g., isostructural $Li_2CoP_2O_7$)[22] and Na-based (e.g., $Na_2FeP_2O_7$, $Na_2CoP_2O_7$) pyrophosphate cathodes.[23,24] These efforts are mostly limited to crystal structure and electrochemical performance. Here, we present a detailed study of the magnetic structure of $Li_2FeP_2O_7$ for the first time. With the presence of multiple Fe sites in close proximity in a pseudolayered structure,[21] $Li_2FeP_2O_7$ forms an interesting compound for magnetic structural analysis. Using temperature-dependent magnetic susceptibility, heat capacity, and neutron powder diffraction study, we have observed an antiferromagnetic ordering with a Néel temperature of T_N = 9 K for $Li_2FeP_2O_7$. The low-temperature neutron diffraction analyses and details of the ground state antiferromagnetic structure of $Li_2FeP_2O_7$ have been described, and by comparing the structural and physical property measurement data, these results have been extended to the isostructural cobalt analogue, $Li_2CoP_2O_7$.

Received: December 21, 2012
Published: February 27, 2013

   dx.doi.org/10.1021/ic302816w | *Inorg. Chem.* 2013, 52, 3334–3341

EXPERIMENTAL SECTION

Material Synthesis. The target compound, $Li_2FeP_2O_7$, was prepared by conventional solid-state synthesis using a stoichiometric 1:1:2 molar mixture of Li_2CO_3 (Wako, 99%), $FeC_2O_4{\cdot}2H_2O$ (Junsei, 99+%), and $(NH_4)_2HPO_4$ (Wako, 99%). These precursors were intimately mixed by wet planetary milling in acetone media for 3 h (400 rpm) employing Cr-hardened stainless steel (Cr-SS) milling media and container. After drying out the acetone, the precursor mixture was ground in an agate mortar, pressed into pellets, and annealed at 600 °C (heating rate = 10 °C/min) for 12 h inside a tube furnace (under Ar flow) to obtain the final $Li_2FeP_2O_7$. The solid-solution $Li_2(Fe_{1-x}Co_x)P_2O_7$ ($x = 0-1$) phases were obtained following a similar procedure by using proportional mixtures of $FeC_2O_4{\cdot}2H_2O$ and CoC_2O_4 (Junsei, 99+%) precursors.

X-ray Diffraction. The powder X-ray diffraction pattern of polycrystalline $Li_2FeP_2O_7$ was collected by a Bruker AXS D8 ADVANCE diffractometer equipped with a Co Kα source (λ_1 = 1.788 97 Å) (operating at 40 mA/35 kV) and a Vantec-1 linear position sensitive detector. The scan was performed in the 2θ range 10−80° (at 0.028° s^{-1}). Rietveld refinement was performed with TOPAS-Academic V4.1 software.[25]

Mössbauer Spectroscopy. Mössbauer analysis was performed with a Topologic System Inc. unit having a ^{57}Co γ-ray source (calibrated with an α-Fe standard) and with MossWinn3.0 software.

Magnetic Susceptibility and Specific Heat Measurement. The magnetic susceptibility measurements of $Li_2(Fe_{1-x}Co_x)P_2O_7$ were conducted with a Quantum Design SQUID magnetometer ($x = 0$) and a Quantum Design physical property measurement system (PPMS) equipped with a vibrating sample magnetometer ($x = 0-1$). The magnetization was recorded in zero field cooled (ZFC) and field cooled (FC) modes with varied applied external magnetic field (H) in the temperature range 2−310 K. Heat capacity measurements were performed on $Li_2FeP_2O_7$ and $Li_2CoP_2O_7$ pellets with a Quantum Design PPMS device in the temperature range 2−310 K.

Neutron Powder Diffraction. Neutron powder diffraction (NPD) experiments were performed at the Institute Laue Langevin (ILL, Grenoble, France) with the D20 high-intensity powder diffractometer with a wavelength of 2.420 Å. The D20 diffractometer has high resolution at low angle, enabling the magnetic structure determination. For the measurements, the sample in form of ~3 g of powder was loaded in a 5-mm-diameter cylindrical vanadium can, and the diffraction patterns were collected between 2 and 300 K with an orange cryostat. The Rietveld analysis[26] and magnetic structure determination were conducted with the FullProf program.[27]

RESULTS AND DISCUSSION

Crystal Structure. X-ray powder diffraction revealed the formation of the desired $Li_2FeP_2O_7$ end product as shown by the Rietveld refinement (Figure 1). The final product contains 98.14% of $Li_2FeP_2O_7$ product phase with minimal impurities ($LiFePO_4$ = 1.3% and $Fe_2P_2O_7$ = 0.56%). The $Li_2FeP_2O_7$ product had a monoclinic structure (space group $P2_1/c$) with the following lattice parameters: a = 11.0201(3) Å, b = 9.7563(3) Å, c = 9.8081(3) Å, β = 101.5(3)°, and V = 1033.18(5) Å^3. All samples across the rest of the $Li_2(Fe_{1-x}Co_x)P_2O_7$ solid solution, up to and including $Li_2CoP_2O_7$, were found to be isostructural by XRD study indicated by similar diffraction patterns with gradual shifting toward higher angle owing to the smaller size of Co (74.5 pm-CoO_6) versus Fe (78 pm-FeO_6).[28] The comparative XRD patterns and corresponding lattice parameters are shown in Figure 2 and Table 1, respectively.

For $Li_2FeP_2O_7$, Mössbauer analysis showed the formation of majority of Fe^{2+} species with negligible Fe^{3+} impurities, adequate for temperature-variable neutron diffraction analysis. The $Li_2FeP_2O_7$ structure consists of a three-dimensional $[FeP_2O_7]_\infty$ network arising from interconnecting

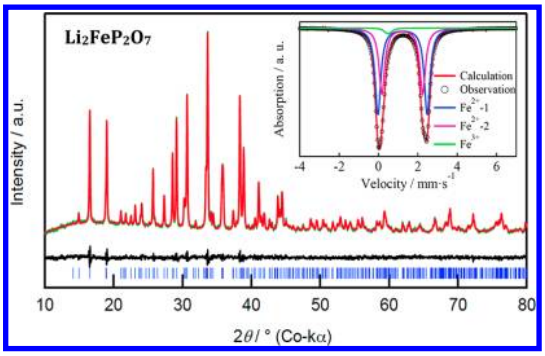

Figure 1. X-ray powder diffraction pattern with Rietveld refinement of solid-state prepared monoclinic $Li_2FeP_2O_7$ compound. The green dots (experimental data points), red line (simulated powder pattern), black line (difference in experimental and simulated patterns), and blue tick marks (Bragg diffraction positions) illustrate a high-purity pyrophosphate product. The reliability factors of the refinement are R_{wp} = 1.502%, R_p = 1.262%, GOF = 1.098, and R_{Bragg} = 2.22%. (Inset) Mössbauer spectrum of $Li_2FeP_2O_7$ powder showing the Fe^{2+} doublets with minimal (~2%) Fe^{3+} peaks.

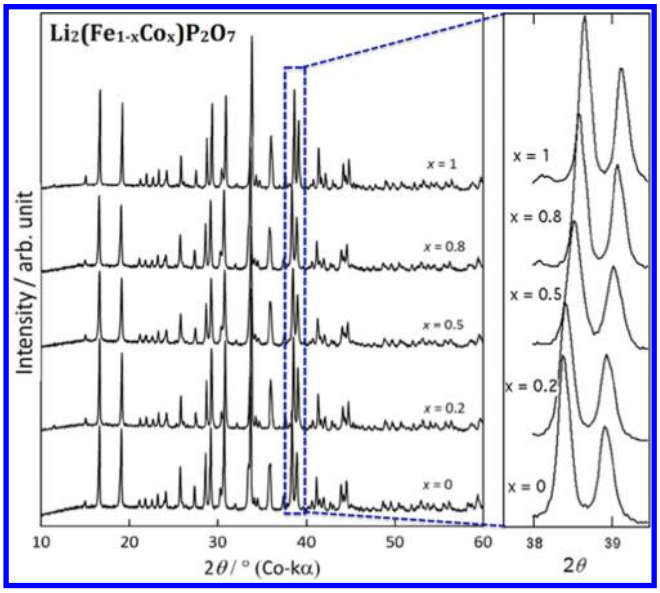

Figure 2. Comparative powder X-ray diffraction patterns of isostructural binary $Li_2(Fe_{1-x}Co_x)P_2O_7$ compounds. With higher Co content, there occurs a gradual peak shifting toward higher 2θ angle owing to the steady lattice shrinking due to the smaller ionic radius of Co vs Fe.

$[Fe_4P_8O_{32}]_\infty$ undulating layers, accommodating the constituent Li atoms at different tunnel sites (Figure 3). The Fe atoms are distributed among three crystallographic sites: a completely filled FeO_6 octahedral site (Fe1) and partially filled FeO_5 trigonal-bipyramidal site (Fe2). The Li species occupy LiO_5 bipyramidal sites, which are partially filled by Fe species (Fe3). The FeO_5 and LiO_5 bipyramids involve Li−Fe antisite defects owing to the close proximity and similar ionic size of Li (76 pm-LiO_6) and Fe (78 pm-FeO_6).[28] The overall structure can be assumed to be a pseudolayered structure with stacking of two-layers of Fe atoms separated by a monolayer of Li atoms, when projected in the ac plane.

Magnetic Susceptibility and Specific Heat of $Li_2FeP_2O_7$. Figure 4 shows the temperature dependence of the magnetization $M(T)$ at T < 50 K for $Li_2FeP_2O_7$ in a FC

dx.doi.org/10.1021/ic302816w | Inorg. Chem. 2013, 52, 3334−3341

Table 1. Lattice Parameters and Unit Cell Volume of $Li_2(Fe_{1-x}Co_x)P_2O_7$ Binary Phases with Monoclinic ($P2_1/c$) Symmetry

materials	a (Å)	b (Å)	c (Å)	β (°)	V (Å^3)
$Li_2FeP_2O_7$	11.0201(3)	9.7563(3)	9.8081(3)	101.53(3)	1033.18(5)
$Li_2(Fe_{0.8}Co_{0.2})P_2O_7$	11.0084(6)	9.7472(1)	9.8008(2)	101.57(2)	1030.24(5)
$Li_2(Fe_{0.5}Co_{0.5})P_2O_7$	10.9923(4)	9.7268(3)	9.7896(4)	101.65(2)	1025.11(3)
$Li_2(Fe_{0.2}Co_{0.8})P_2O_7$	10.9763(1)	9.7093(6)	9.771(2)	101.68(8)	1020.21(4)
$Li_2CoP_2O_7$	10.9615(8)	9.6965(3)	9.7648(1)	101.78(6)	1016.0(2)

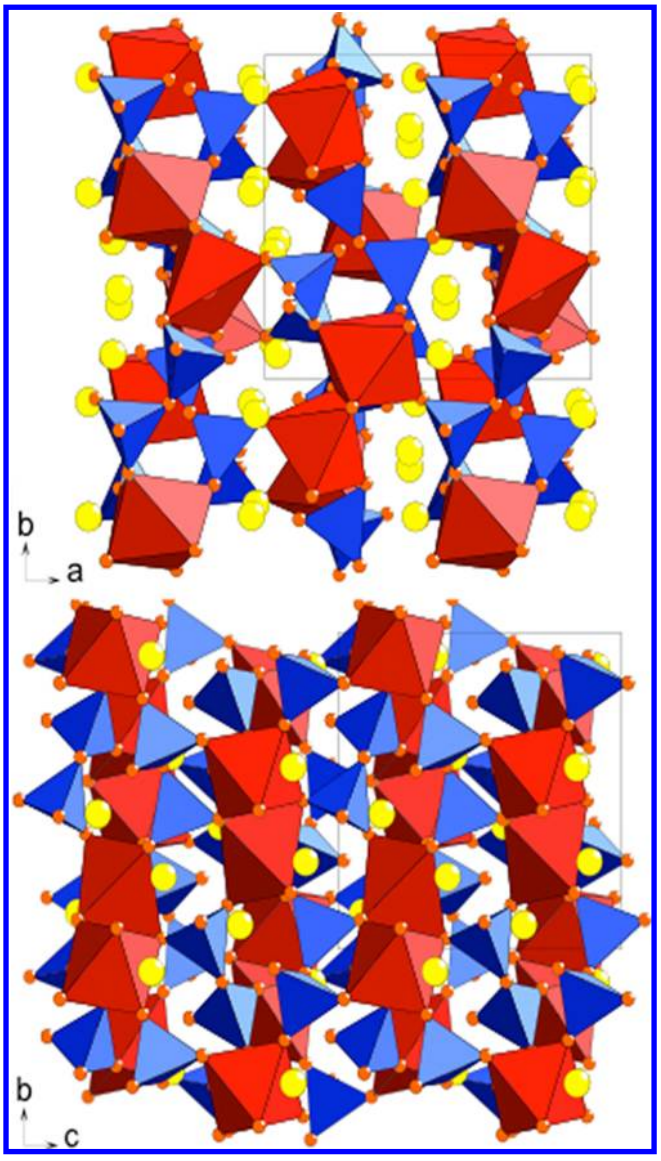

Figure 3. Crystallographic structure of $Li_2FeP_2O_7$ pyrophosphate compound projected in the (top) *ab* plane and (bottom) *bc* plane. Fe1 and Fe2 polyhedra are red, O atoms are orange, Li atoms are yellow balls (except Li5/Fe3 which is green), and PO_4 tetrahedra are blue in color.

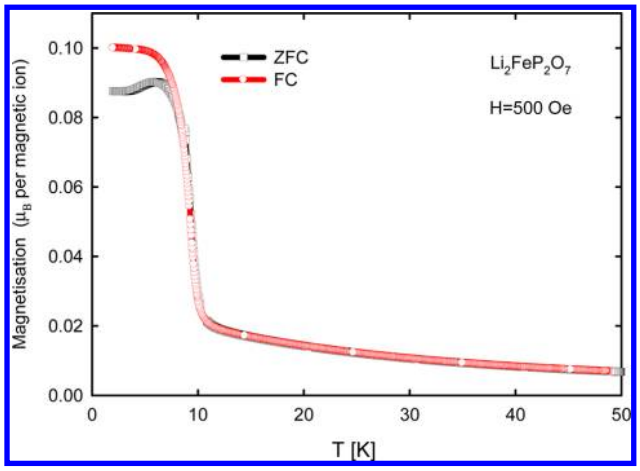

Figure 4. Temperature dependence of the magnetization M of $Li_2FeP_2O_7$ measured in the zero field cooled (ZFC) and field cooled (FC) modes under a magnetic field H = 500 Oe.

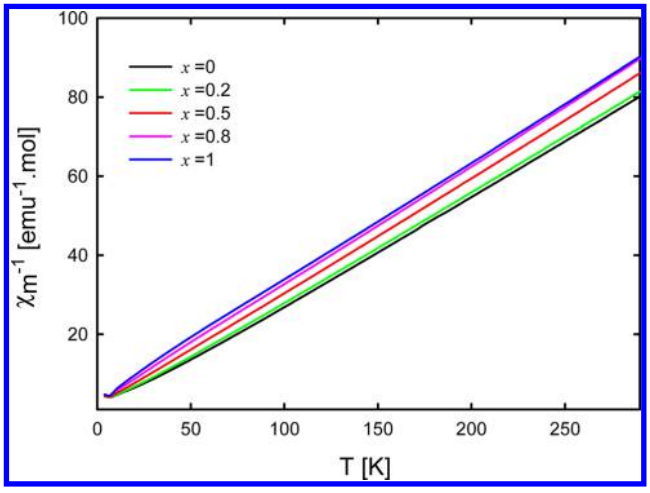

Figure 5. Temperature dependence of inverse magnetic susceptibilities for samples across the $Li_2(Fe_{1-x}Co_x)P_2O_7$ solid solution, measured under a magnetic field H = 10 000 Oe.

sequence and a ZFC sequence in a field of H = 500 Oe. The resulting curve is similar to what was observed previously.[29] A magnetic transition clearly occurs at $T_N \sim 9$ K. A substantial increase is observed below the transition temperature with a weak ferromagnetic component indicated by the significant difference between the FC and ZFC measurements.

Figure 5 shows the inverse magnetic susceptibility as a function of temperature across the $Li_2(Fe_{1-x}Co_x)P_2O_7$ phase diagram. All compositions show Curie–Weiss (paramagnetic) behavior for $T > 50$ K; i.e., the magnetic susceptibility $\chi = M/H$ follows the following law: $\chi(T) = \chi_0 + C/(T - \Theta_{CW})$ where χ_0 accounts for a temperature-independent susceptibility. Table 2 lists parameters derived from Curie–Weiss fits to each of the curves above 50 K. The value of the Curie constant ($C \approx \mu_{eff}^2/8$ in cgs units) extracted from the fit for $Li_2FeP_2O_7$ gives an effective moment μ_{eff} = 5.29 μ_B/Fe, somewhat higher than the theoretical value of 4.89 for high-spin Fe^{2+} (d^6, $t_{2g}^4e_g^2$, $S = 2$), but not unusual for Fe^{2+} oxides with imperfectly quenched orbital contributions; for example, a value of 5.20 μ_B was found in single-crystals of $LiFePO_4$ with the same Fe^{2+} oxidation state.[30] A similar discrepancy observed for $Li_2CoP_2O_7$ (μ_{eff} = 5.17 μ_B/Co vs μ_{theor} = 3.87 μ_B/Co) is typical for high-spins Co^{2+} oxides, and the trend is repeated for the solid-solution phases (Table

dx.doi.org/10.1021/ic302816w | Inorg. Chem. 2013, 52, 3334–3341

Table 2. Parameters Derived from Curie–Weiss Fit to Magnetic Susceptibility Data above 50 K for $Li_2(Fe_{1-x}Co_x)P_2O_7$

x	χ_0 ($\times 10^{-3}$ emu/mol)	C_M*(emu K/mol)	Θ_{CW} (K)	μ_{eff} (μ_B)	μ_{theor} (μ_B)
0.0	−1.7	3.502	8.8	5.29	4.89
0.2	−2.19	3.550	1.6	5.33	4.70
0.5	−6.35	3.482	−6.2	5.28	4.39
0.8	−1.44	3.326	−8.7	5.16	4.04
1.0	0.43	3.343	−11.5	5.17	3.87

2). The Curie–Weiss temperature Θ_{CW} evolves from a slightly positive value (8.8 K) for x = 0, $Li_2FeP_2O_7$, to a slightly negative value (−11.5 K) for x = 1, $Li_2CoP_2O_7$. This compares reasonably well to the previously reported value of Θ_{CW} = 11.5 for $Li_2FeP_2O_7$.[29] Such a signal is typical of either canted antiferromagnetic structures, where the spins are not perfectly antiparallel, or ferrimagnetic structures in which two sublattices exhibit slightly different magnetic moments; i.e., of the presence in the former case of both ferromagnetic (FM) and antiferromagnetic (AFM) exchange interactions. FM slightly dominates for $Li_2FeP_2O_7$, and AFM for $Li_2CoP_2O_7$, but (as can be seen in Figure 5) the net behavior appears to be fundamentally identical.

Figure 6 shows FC and ZFC magnetization for $Li_2CoP_2O_7$, measured under an applied field H = 500 Oe. The similar

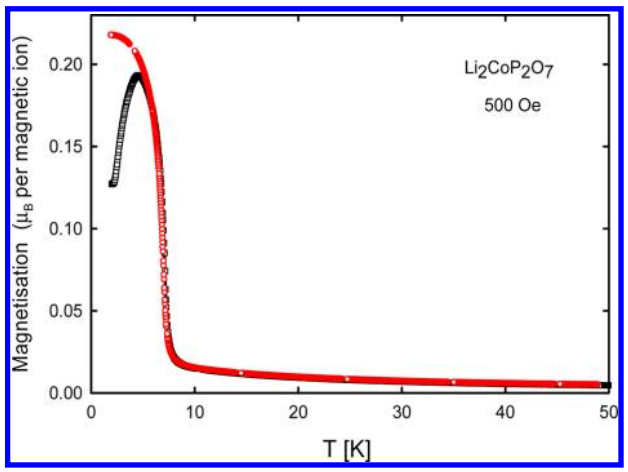

Figure 6. Temperature dependence of the magnetization M of $Li_2CoP_2O_7$ measured in the zero field cooled (ZFC) and field cooled (FC) modes under a magnetic field H = 500 Oe.

behavior to that of $Li_2FeP_2O_7$ (Figure 4), with a divergence below ~7 K indicating the appearance of a weak FM moment, further suggests that these two phases contain essentially the same magnetic exchange interactions. The specific heat curves for $Li_2FeP_2O_7$ and $Li_2CoP_2O_7$ shown in Figure 7 are also consistent with this, with both phases showing λ-type anomalies, at 9 and 6.8 K, respectively, indicating the onset of long-range magnetic ordering at these temperatures. Finally, Figure 8 shows the magnetic field dependence of magnetization $M(H)$ for all samples at 2 K. A hysteresis loop opens up for all samples, confirming the presence of an FM component, which shows a continuous but modest evolution across the binary $Li_2(Fe_{1-x}Co_x)P_2O_7$ solid solutions.

Figure 9 displays the magnetic susceptibility of $LiFeP_2O_7$, which was obtained from the chemical oxidation of the pristine

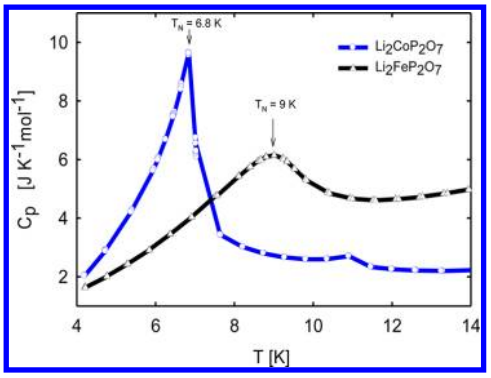

Figure 7. Specific heat capacity as a function of temperature for $Li_2FeP_2O_7$ and $Li_2CoP_2O_7$.

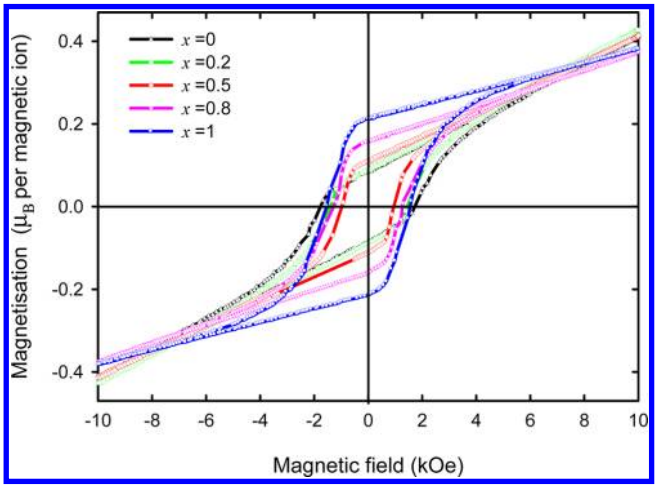

Figure 8. Field dependence of magnetization for samples across the $Li_2(Fe_{1-x}Co_x)P_2O_7$ solid solution, measured at 2 K.

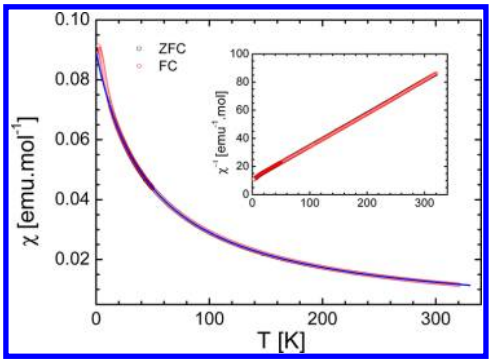

Figure 9. Temperature dependence of the magnetic susceptibility χ of $LiFeP_2O_7$ (chemically oxidized) measured in the zero field cooled and field cooled modes under a magnetic field H = 10 000 Oe. The blue line shows a fit to the Curie–Weiss law. Inset: Inverse susceptibility as a function of temperature.

$Li_2FeP_2O_7$ compound. $\chi(T)$ does not show any signature of a long-range order down to 2 K. Furthermore, the FC and ZFC measurements are perfectly superimposed which also exclude short-range order. As shown by the inset of Figure 9 which plots $1/\chi$ versus T, the susceptibility follows a Curie–Weiss law and only deviates from it at T < 10 K, which can be explained by the presence of residual $Li_2FeP_2O_7$ phase. The experimental value of the effective moment, 5.88 μ_B/Fe, is in perfect accordance with the theoretical value of 5.91 μ_B/Fe for high-

dx.doi.org/10.1021/ic302816w | Inorg. Chem. 2013, 52, 3334–3341

spin Fe^{3+} (d^5, $t_{2g}^3e_g^2$, $S = {}^5/_2$). The value of $\theta = -48.5$ K indicates moderate antiferromagnetic exchange interactions as compared to the weak interactions in $Li_2FeP_2O_7$.

Magnetic Structure from Neutron Powder Diffraction Measurements. A neutron diffraction experiment at room temperature confirmed the nuclear structure as already published.[22] Note that as D20 is a powder diffractometer dedicated to magnetic structure determination, it presents a good resolution at low angle and a large wavelength; as a consequence, the patterns are not suited to structure determination. The Rietveld refinement of the pattern recorded at 150 K with the structural model[18] is presented in Figure 10a.

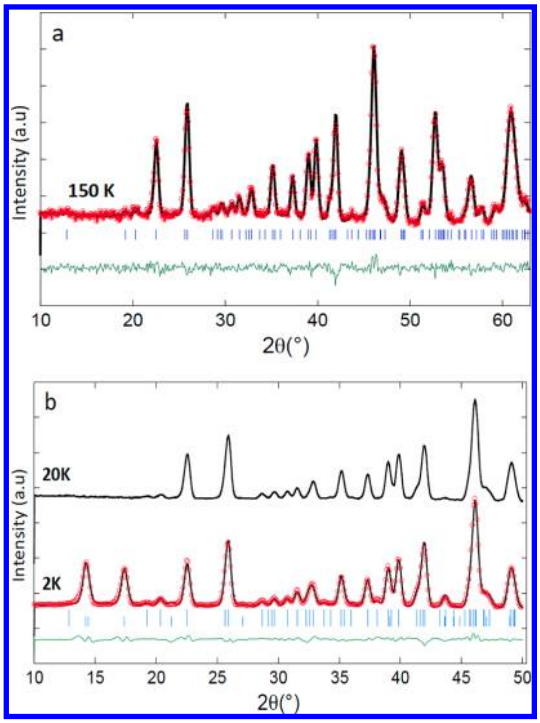

Figure 10. (a) Rietveld refinement of the neutron powder pattern of $Li_2FeP_2O_7$ at 150 K (D20 diffractometer, $\lambda = 2.42$ Å). Red dots, black and green line, blue vertical tick marks represent the observed, calculated, difference pattern and Bragg peaks, respectively. (b) Rietveld refinement of the neutron powder diffraction pattern at 2 K. Red dots, black and green line, blue vertical tick marks represent the observed, calculated, difference pattern and Bragg peaks (1st line, nuclear; 2nd line, magnetic), respectively. The pattern at 20 K (above T_N) is shown for comparison.

From room temperature to 1.7 K, we did not observe any change in the intensities and position of the nuclear peaks, except what is expected from a slight thermal contraction. This observation indicates the absence of any structural transition down to 1.7 K. For temperatures below $T_N = 9$ K (Figure 10b), we note the appearance of extra peaks in the neutron diffraction pattern that are of purely magnetic origin (see Figure 11). These peaks can be indexed in the same unit cell as the nuclear structure, meaning that the propagation vector is $\mathbf{k} = (0,0,0)$. The Shubnikov group is therefore the same as the nuclear one, $P2_1/c$. We performed a symmetry analysis[31] to get the possible magnetic structures. Within the nuclear space group $P2_1/c$ and considering one iron atom in the general 4*e* Wyckoff position, a propagation vector $\mathbf{k} = (0,0,0)$ leads to a representation $\Gamma_{magnetic} = 3\Gamma_1 + 3\Gamma_2 + 3\Gamma_3 + 3\Gamma_4$. The basis vectors related to each representation are gathered in Table 3.

We tested the different possible representations using simulated annealing techniques[32] as implemented in the FullProf program. The three iron atoms of the nuclear cell, Fe1, Fe2, and Fe3, the two latter with partial occupancy, are taken into account in the magnetic structure. Attempts with magnetic moments located on Fe1 only could not successfully account for the observed magnetic peaks. We analyzed the different representations and found that magnetic moments follow the Γ_1 representation. When doing the simulated annealing refinement, we realized that moments on Fe1 and Fe3 were always parallel to the [100] direction, while moments on Fe2 lie in the *ac*-plane even if the initial configuration was random. Our final refinement took this constraint into account. Moments were also constrained at the same absolute value for each three iron atoms, and the refined value is 3.54(1) μ_B, in agreement with susceptibility measurement and what is commonly observed for high spin Fe^{2+} (d^6, $t_{2g}^4e_g^2$, $S = 2$).[33−37] The final Rietveld refinement is shown in Figure 10b, and the list of magnetic moments within the unit cell is given in Table 4. The series of patterns between 1.7 and 20 K have been refined. The magnetic structure is obviously the same for all patterns except a decrease in the magnetic moment, which falls to zero as the temperature increases to T_N. This variation is illustrated in Figure 12.

Figure 13 presents a view of the magnetic structure. For reasons of clarity, we have only represented iron atoms and their environment (octahedral for Fe1 and trigonal-bypiramid for Fe2 and Fe3, the latter being mixed sites with Li). Iron atoms are arranged in kinds of clusters made of one FeO_6 octahedra and two FeO_5 bypiramids linked through edges, and these clusters are linked through vertices to form layers running along the [010] direction. Of course, as Fe2 and Fe3 are mixed with Li, some clusters will statistically contain from 1 to 3 iron atoms, the site occupied by Fe2 and Fe3 being occupied also by Li atoms. Our picture in Figure 13 is a view of a hypothetical magnetic structure where clusters are fully occupied by iron. We can see that, within a cluster, moments of iron atoms are almost parallel (i.e., ferromagnetically coupled), and clusters are coupled antiferromagnetically along the direction of the chains. From one chain to another, chains are ferromagnetically coupled. If Fe1 and Fe3 present magnetic moments along *a* only, Fe2 presents moments oriented in the *a*,*c*-plane.

Let us now reconsider the magnetic structure together with the macroscopic measurements. The proposed magnetic structure from neutron diffraction is antiferromagnetic, which is in contradiction with susceptibility measurements identifying a small net ferromagnetic component of ∼0.2 μ_B per formula unit (see Figures 4 and 8). Actually, the Γ_1 representation allows a ferromagnetic component along *b*, which was fixed to zero in the refinement procedure. Refining that *b* component while keeping a fixed moment of 3.54(1) μ_B for all Fe^{2+} does not modify the magnetic intensity on the two main reflections seen at $2\theta = 14.2°$ and 17.3°. Therefore, from powder diffraction, we are limited to refine an accurate value of the magnetic moment along the *b*-axis even though we should expect one. As a consequence, the magnetic order proposed in Figure 13 is not but is close to the real structure, which should exhibit a small ferromagnetic component. Neutron powder diffraction on single crystals, if available, should lift this uncertainty.

In Figure 14, we have plotted the Fe−Fe bonds in order to easily figure out how irons are connected to each other, in order to figure out why the magnetic structure is not collinear. We

dx.doi.org/10.1021/ic302816w | Inorg. Chem. 2013, 52, 3334−3341

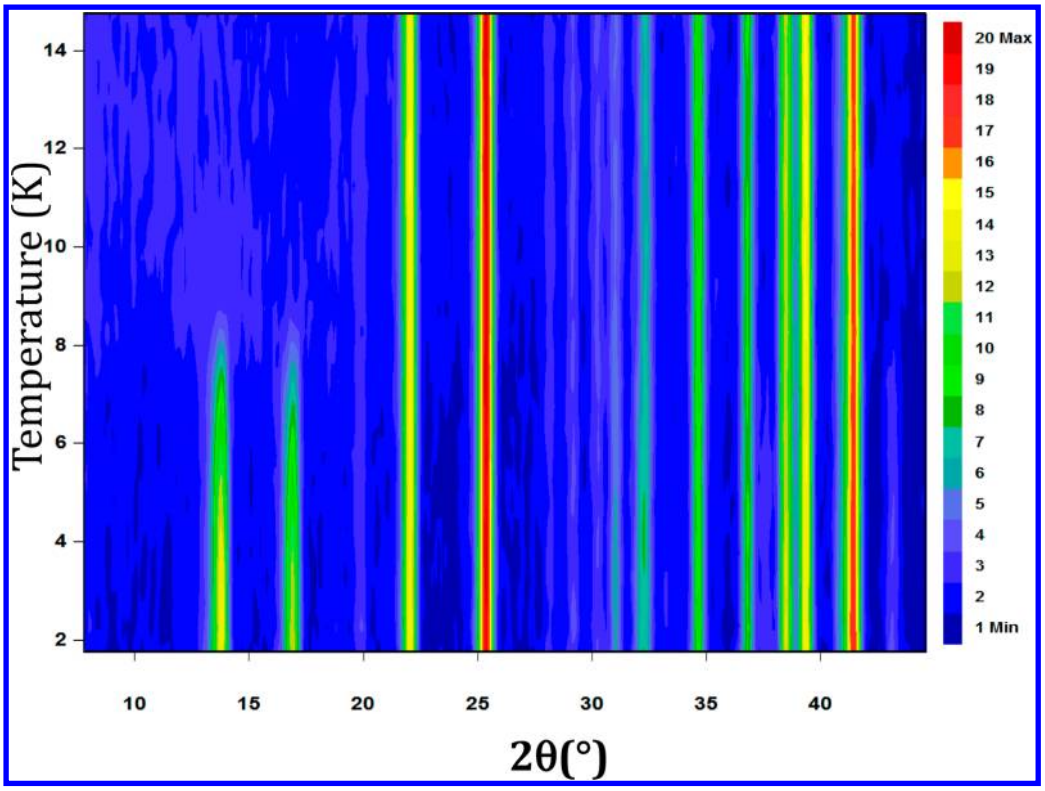

Figure 11. 2D plot of the neutron diffraction patterns of $Li_2FeP_2O_7$ versus temperature (D20 diffractometer, λ = 2.42 Å). Note the apparition of magnetic peaks below T_N = 9 K.

Table 3. Representation Analysis for a Magnetic Atom in the 4*e* Wyckoff Position of Space Group $P2_1/c$ and a Propagation Vector k = (0,0,0)[a]

Fe_1 x, y, z	Fe_2 $-x, y + {}^1/_2, -z + {}^1/_2$	Fe_3 $-x, -y, -z$	Fe_4 $x, -y + {}^1/_2, z + {}^1/_2$
	Γ_1 (G_X, F_Y, G_Z)		
(1 0 0)	(−1 0 0)	(1 0 0)	(−1 0 0)
(0 1 0)	(0 1 0)	(0 1 0)	(0 1 0)
(0 0 1)	(0 0 −1)	(0 0 1)	(0 0 −1)
	Γ_2 (A_X, C_Y, A_Z)		
(1 0 0)	(−1 0 0)	(−1 0 0)	(1 0 0)
(0 1 0)	(0 1 0)	(0 −1 0)	(0 −1 0)
(0 0 1)	(0 0 −1)	(0 0 −1)	(0 0 1)
	Γ_3 (F_X, G_Y, F_Z)		
(1 0 0)	(1 0 0)	(1 0 0)	(1 0 0)
(0 1 0)	(0 −1 0)	(0 1 0)	(0 −1 0)
(0 0 1)	(0 0 1)	(0 0 1)	(0 0 1)
	Γ_4 (C_X, A_Y, C_Z)		
(1 0 0)	(1 0 0)	(−1 0 0)	(−1 0 0)
(0 1 0)	(0 −1 0)	(0 −1 0)	(0 1 0)
(0 0 1)	(0 0 1)	(0 0 −1)	(0 0 −1)

[a]Basis vectors corresponding for each representation are explicit.

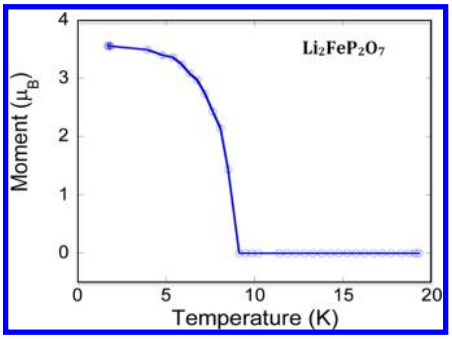

Figure 12. Variation of the intensity of the magnetic moments on iron atoms in $Li_2FeP_2O_7$ as a function of temperature, deduced from the Rietveld refinement of neutron powder diffraction patterns.

consider two configurations: Fe1, Fe2, and Fe3 occupied by iron and only Fe1 and Fe2 occupied by iron. We can see for the former case that this induces triangular interactions between clusters, but the magnetic structure does not show any sign of resulting frustration. This is in agreement with the ratio $|\Theta_{CW}|/T_N$ close to 1. Looking at the topology when iron is only distributed on the Fe1 and Fe2 sites creates some dimers that consist of two almost parallel magnetic moments, which are

Table 4. Magnetic Structure of $Li_2FeP_2O_7$ As Refined against Neutron Powder Diffraction Pattern at 2 K[a]

atom	position	position	position	occupation factor	M_X	M_Y	M_Z	M_{total}
Fe1	0.672	0.572	0.698	1	3.54(1)	0	0	3.54(1)
Fe2	0.821	0.286	0.752	0.66667	2.90(1)	0	2.68(1)	3.54(1)
Fe3	0.039	0.076	0.656	0.33333	−3.54(1)	0	0	3.54(1)

[a]Moments follow the Γ_1 representation and are expressed in μ_B. Note that we cannot refine an M_Y value with accuracy from the neutron powder diffraction data; therefore, we fixed in to zero (see text).

dx.doi.org/10.1021/ic302816w | *Inorg. Chem.* 2013, 52, 3334−3341

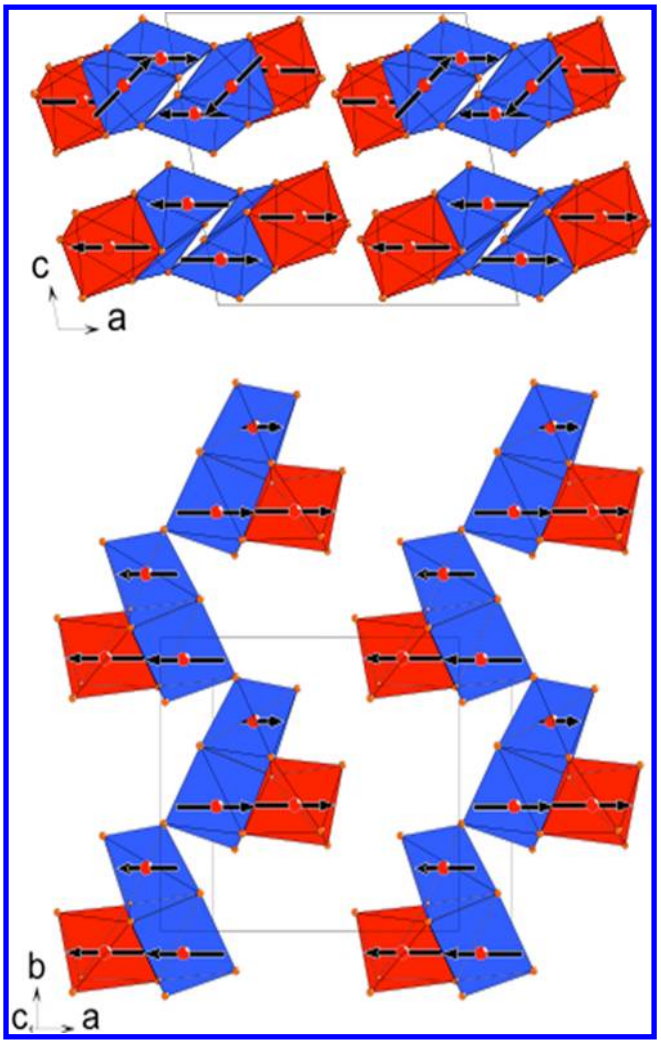

Figure 13. Representation of the magnetic structure of $Li_2FeP_2O_7$. Arrows correspond to magnetic moments on the iron atoms. Fe1 sits in the middle of red octahedra; Fe2 and Fe3 sit in the middle of $^2/_3$ and $^1/_3$ of blue trigonal bipyramids, respectively. Fe1 and Fe3 follow the Γ_1 (G_X, 0, 0) representation while Fe2 follows the same representation but with a component along z: Γ_1 (G_X, 0, G_Z). For reasons of clarity, PO_4 groups and Li atoms are not shown.

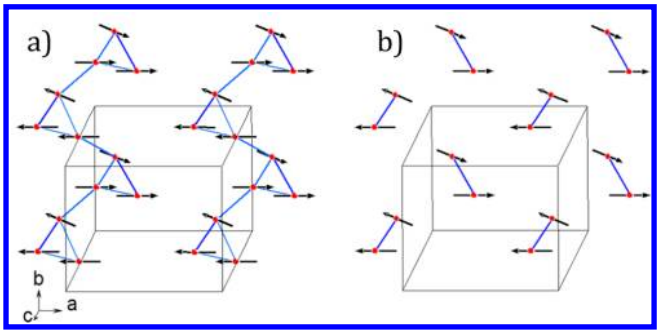

Figure 14. Topology of $Li_2FeP_2O_7$. Fe atoms are linked to show the different interaction paths: (a) Fe1, Fe2, and Fe3; (b) Fe1 and Fe2 only (Fe3 not taken into account as mainly occupied by Li atoms).

antiferromagnetically coupled. This means that the interaction via PO_4 groups, so leading to supersuperexchange interactions, has a strong influence and cannot be neglected in front of the superexchange interactions.

Taking into account the Goodenough–Kanamori–Anderson principles for superexchange interaction between two neighboring Fe^{2+}-ions with partially occupied orbitals (i.e., d^6–d^6 interaction), the spin–spin coupling can be correlated to the cation–anion–cation (i.e., Fe^{2+}–O^{2-}–Fe^{2+}) orientation.[38−40] When this angle is close to 90°, the superexchange interaction is ferromagnetic, while angles closer to 180° favor antiferromagnetic superexchange. The $Li_2FeP_2O_7$ crystal and magnetic structures are consistent with this principle. In the individual FeO_6–FeO_5 clusters, the Fe^{2+}–O^{2-}–Fe^{2+} bond angles range from 92° to 99° and lead to ferromagnetic coupling, whereas the adjacent clusters with larger Fe^{2+}–O^{2-}–Fe^{2+} bond angle (∼111°) stabilize into antiferromagnetic coupling (Figures 13 and 14). Further, the overall open framework structure with isolated FeO_x polyhedra in $Li_2FeP_2O_7$ leads to a lesser degree of orbital overlap, weakening the superexchange interaction and thereby lowering the antiferromagnetic ordering temperature. This explains the low T_N value of 9 K in $Li_2FeP_2O_7$, compared to other Li-ion insertion compounds such as $LiFePO_4$ (T_N = 52 K)[35] and $LiFeSO_4F$ (T_N = 25 K).[36]

Finally, with respect to the magnetic structure of $Li_2CoP_2O_7$, we note that while the electronic configuration of Co^{2+} (d^7, t_{2g}^5, e_g^2, $S = {}^3/_2$) leads to a smaller moment than that of Fe^{2+}, the population of the e_g orbitals responsible for superexchange interactions is identical. This explains the qualitatively identical magnetic behavior observed across the $Li_2(Fe_{1-x}Co_x)P_2O_7$ solid solution, and strongly indicates that the same magnetic structure is adopted throughout.

■ CONCLUSIONS

In this Article, we have reported the magnetic structure of the 3.5 V $Li_2FeP_2O_7$ cathode compound. Neutron diffraction reveals a complex ordering scheme below T_N = 9 K involving antiferromagnetic interactions among ferromagnetic clustered units. The magnetic moments on Fe1 and Fe3 are parallel to [100] while the moment on Fe2 is in the *ac*-plane, which (in combination with partial occupancy of Fe sites by Li) permits a weak net ferromagnetic moment that can be seen in magnetic property measurements below T_N. Magnetic susceptibility, heat capacity, and magnetization measurements are consistent with the neutron diffraction results and show no significant changes across the $Li_2(Fe_{1-x}Co_x)P_2O_7$ solid solution other that those expected due to the different magnetic moments of Fe^{2+} and Co^{2+}. They support the onset of the same type of long-range magnetic ordering in $Li_2CoP_2O_7$ at T_N = 6.8 K.

■ AUTHOR INFORMATION

Corresponding Author

*E-mail: prabeer@chemsys.t.u-tokyo.ac.jp. Phone: +81-3-5841-7295. Fax: +81-3-5841-7488.

Author Contributions

⊥Authors with equal contribution.

Notes

The authors declare no competing financial interest.

■ ACKNOWLEDGMENTS

We thank S. Nishimura and S. C. Chung for fruitful discussions. P.B. acknowledges the Japan Society for the Promotion of Sciences for a JSPS Fellowship, and T.Y. is grateful to Panasonic Inc. for a Panasonic Scholarship at the University of Tokyo. We appreciate the financial support of "Element

Strategy Initiative for Catalysts & Batteries (ESICB)" by the Ministry of Education, Culture, Sports, Science and Technology (MEXT). G.R. thanks T. Hansen for help in neutron measurements and ILL for allocated beam time. C.D.L. thanks the Australian Research Council (DP110102662) for financial support.

REFERENCES

(1) Etacheri, V.; Marom, R.; Elazari, R.; Salitra, G.; Aurbach, D. *Energy Environ. Sci.* **2011**, *4*, 3243−3262.
(2) Bruce, P. G.; Scrosati, B.; Tarascon, J. M. *Angew. Chem., Int. Ed.* **2008**, *47*, 2930−2946.
(3) Desilvestro, J.; Haas, O. *J. Electrochem. Soc.* **1990**, *137*, 5−22.
(4) Yabuuchi, N.; Ohzuku, T. *J Power Sources* **2003**, *119*, 171−174.
(5) Padhi, A. K.; Nanjundaswamy, K. S.; Goodenough, J. B. *J. Electrochem. Soc.* **1997**, *144*, 1188−1194.
(6) Yamada, A.; Chung, S. C.; Hinokuma, K. *J. Electrochem. Soc.* **2001**, *148*, 224−229.
(7) Yamada, A.; Hosoya, M.; Chung, S. C.; Kudo, Y.; Hinokuma, K.; Liu, K. Y.; Nishi, Y. *J. Power Sources* **2003**, *119*, 232−238.
(8) Tarascon, J. M.; Recham, N.; Armand, M.; Chotard, J. N.; Barpanda, P.; Walker, W.; Dupont, L. *Chem. Mater.* **2010**, *22*, 724−739.
(9) Yamada, A.; Iwane, N.; Harada, Y.; Nishimura, S.; Koyama, Y.; Tanaka, I. *Adv. Mater.* **2010**, *22*, 3583−3587.
(10) Nyten, A.; Abouimrane, A.; Armand, M.; Gustafsson, T.; Thomas, J. O. *Electrochem. Commun.* **2005**, *7*, 156−160.
(11) Ramesh, T. N.; Lee, K. T.; Ellis, B. E.; Nazar, L. F. *Electrochem. Solid-State Lett.* **2010**, *13*, 43−47.
(12) Recham, N.; Chotard, J. N.; Dupont, L.; Delacourt, C.; Walker, W.; Armand, M.; Tarascon, J. M. *Nat. Mater.* **2010**, *9*, 68−74.
(13) Barpanda, P.; Ati, M.; Melot, B. C.; Rousse, G.; Chotard, J. N.; Doublet, M. L.; Sougrati, M. T.; Corr, S. A.; Jumas, J. C.; Tarascon, J. M. *Nat. Mater.* **2011**, *10*, 772−779.
(14) Barpanda, P.; Nishimura, S.; Yamada, A. *Adv. Energy Mater.* **2012**, *2*, 841−859.
(15) Padhi, A. K.; Nanjundaswamy, K. S.; Masquelier, C.; Okada, S.; Goodenough, J. B. *J. Electrochem. Soc.* **1997**, *144*, 1609−1613.
(16) Lee, S.; Park, S. S. *Chem. Mater.* **2012**, *24*, 3550−3557.
(17) Clark, J. M.; Nishimura, S.; Yamada, A.; Islam, M. S. *Angew. Chem., Int. Ed.* **2012**, *51*, 13149−13153.
(18) Nishimura, S. I.; Nakamura, M.; Natsui, R.; Yamada, A. *J. Am. Chem. Soc.* **2010**, *132*, 13596−13597.
(19) Barpanda, P.; Ye, T.; Chung, S. C.; Yamada, Y.; Nishimura, S.; Yamada, A. *J. Mater. Chem.* **2012**, *22*, 13455−13459.
(20) Furuta, N.; Nishimura, S.; Barpanda, P.; Yamada, A. *Chem. Mater.* **2012**, *24*, 1055−1061.
(21) Shimizu, D.; Nishimura, S.; Barpanda, P.; Yamada, A. *Chem. Mater.* **2012**, *24*, 2598−2603.
(22) Kim, H.; Lee, S.; Park, Y. U.; Kim, H.; Kim, J.; Jeon, S.; Kang, K. *Chem. Mater.* **2011**, *23*, 3930−3937.
(23) Barpanda, P.; Ye, T.; Nishimura, S. I.; Chung, S. C.; Yamada, Y.; Okubo, M.; Zhou, H.; Yamada, A. *Electrochem. Commun.* **2012**, *24*, 116−119.
(24) Barpanda, P.; Avdeev, M.; Ling, C. D.; Lu, J.; Yamada, A. *Inorg. Chem.* **2013**, *52*, 395−401.
(25) Coelho, A. *TOPAS-Academic Version 4.1 Computer Software*; Coelho Software: Brisbane, Australia, 2007.
(26) Rietveld, H. M. *J. Appl. Crystallogr.* **1969**, *2*, 65−71.
(27) Rodriguez-Carvajal, J. *Physica B* **1993**, *192*, 55−69.
(28) Shannon, R. D. *Acta Crystallogr.* **1976**, *A32*, 751−755.
(29) Zhou, H.; Upreti, S.; Chernova, N. A.; Hautier, G.; Ceder, G.; Whittingham, M. S. *Chem. Mater.* **2010**, *23*, 293−300.
(30) Liang, G.; Park, K.; Li, J.; Benson, R. E.; Vaknin, D.; Markert, J. T.; Croft, M. C. *Phys. Rev. B* **2008**, *77*, 064414−064425.
(31) Bertaut, E. F. *Acta Crystallogr., Sect. A* **1968**, *A24*, 217−222.
(32) Kirkpatrick, S.; Gelatt, C. D.; Vecchi, M. P. *Science* **1983**, *220*, 671−680.
(33) Rousse, G.; Rodriguez-Carvajal, J.; Wurm, C.; Masquelier, C. *Chem. Mater.* **2001**, *13*, 4527−4536.
(34) Rousse, G.; Rodriguez-Carvajal, J.; Wurm, C.; Masquelier, C. *Solid State Sci.* **2002**, *4*, 973−978.
(35) Rousse, G.; Rodriguez-Carvajal, J.; Patoux, S.; Masquelier, C. *Chem. Mater.* **2003**, *15*, 4082−4090.
(36) Melot, B. C.; Rousse, G.; Chotard, J. N.; Ati, M.; Rodriguez-Carvajal, J.; Kemei, M. C.; Tarascon, J. M. *Chem. Mater.* **2011**, *23*, 2922−2930.
(37) Melot, B. C.; Rousse, G.; Chotard, J. N.; Kemei, M. C.; Rodriguez-Carvajal, J.; Tarascon, J. M. *Phys. Rev. B* **2012**, *85*, 4415−4415.
(38) Goodenough, J. B. *Phys. Rev.* **1960**, *117*, 1442−1451.
(39) Kanamori, J. *J. Phys. Chem. Solids.* **1959**, *10*, 87−98.
(40) Anderson, P. W. *Phys. Rev.* **1950**, *79*, 350−356.